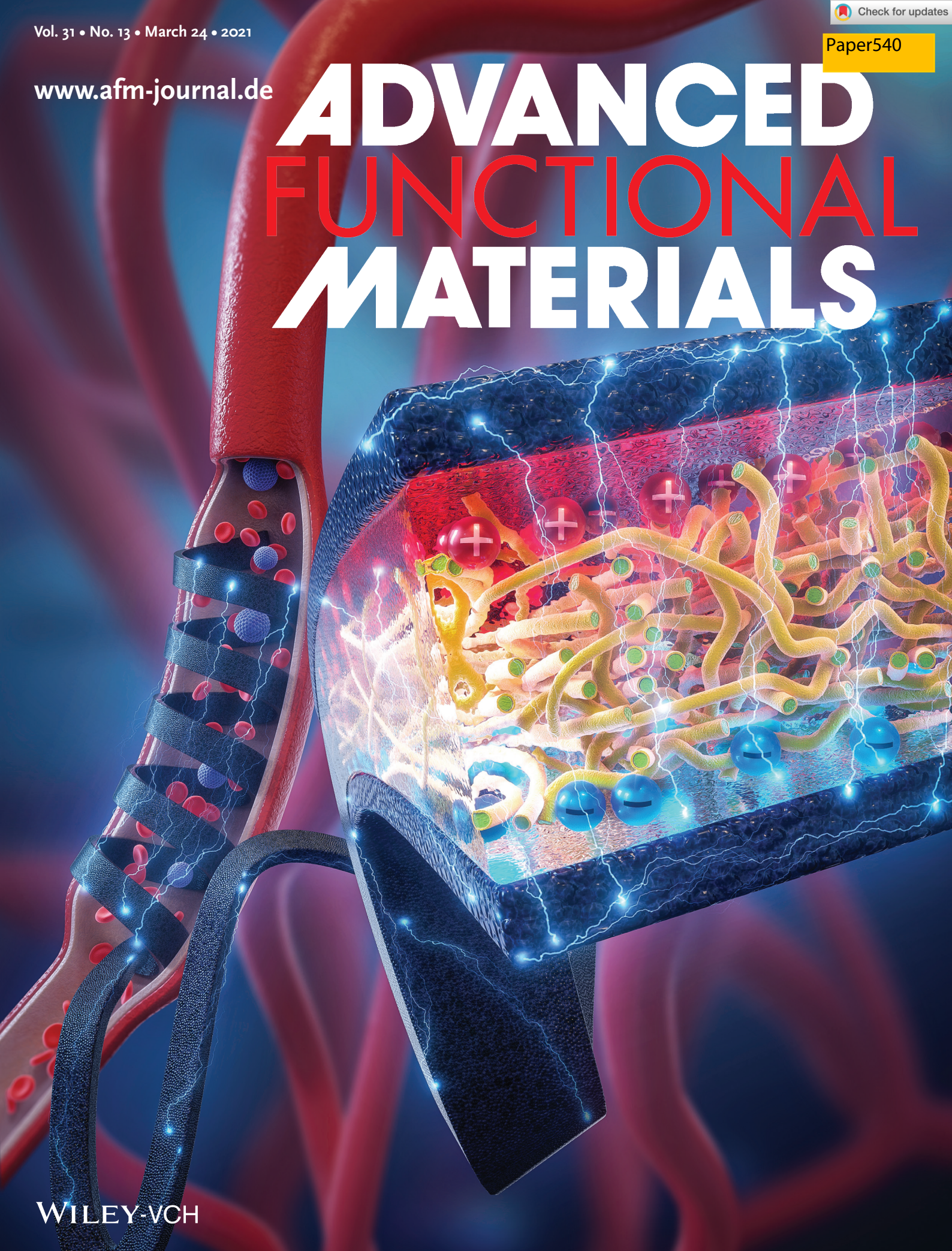


www.afm-journal.de

ADVANCED FUNCTIONAL MATERIALS



Ultralow Voltage High-Performance Bioartificial Muscles Based on Ionically Crosslinked Polypyrrole-Coated Functional Carboxylated Bacterial Cellulose for Soft Robots

Fan Wang, Qinchuan Li,* Jong-Oh Park,* Shaohui Zheng, and Eunpyo Choi*

The development of ultralow voltage high-performance bioartificial muscles with large bending strain, fast response time, and excellent actuation durability is highly desirable for promising applications such as soft robotics, active biomedical devices, flexible haptic displays, and wearable electronics. Herein, a novel high-performance low-priced bioartificial muscle based on functional carboxylated bacterial cellulose (FCBC) and polypyrrole (PPy) nanoparticles is reported, exhibiting a large bending strain of 0.93%, long actuated bending durability (96% retention for 5 h) under an ultralow harmonic input of 0.5 V, broad frequency bandwidth up to 10 Hz, fast response time (≈ 4 s) in DC responses, high energy density (6.81 kJ m^{-3}), and high power density (5.11 kW m^{-3}), all of which mainly stem from its high surface area and porosity, large specific capacitance, tuned mechanical properties, and strong ionic interactions of cations and anions in ionic liquid with FCBC and PPy nanoparticles. More importantly, bioinspired applications such as the grapple robot, bionic medical stent, bionic flower, and wings-vibrating have been realized. These successful demonstrations offer a viable means for developing high-performance bioartificial muscles for next-generation soft bioelectronics including bioinspired robotics, biomedical microdevices, and wearable electronics.

1. Introduction

In the past decades, artificial muscles, which can change their shapes or sizes in response to external stimuli, have received enormous interest in their important applications, such as soft robotics, stretchable flexible electronics, haptic feedback devices, and medical electronic products.^[1–5] Among typical artificial muscles, ionic electroactive polymer (IEAP) actuators have been extensively investigated due to their flexibility, lightweight, facile processability, and relatively large bending deformation and fast response time.^[6–10] Recently, many research groups have developed series of IEAP actuators based on different electrodes, where polyvinylidene fluoride (PVDF) and nafion are commonly used as ionic electrolyte membranes, as shown in Table S1, Supporting Information. However, we find that the PVDF-based actuators and nafion-based actuators showed low bending strains, whose the maximum values are 0.52% (2.5 V, 0.1 Hz) and 0.68% (1.0 V,

0.1 Hz), respectively (Table S1, Supporting Information). Furthermore, these PVDF or nafion-based ionic actuators have other problems such as high cost, environmental unfriendliness, no biocompatibility or biodegradability, and low repeatability of these designed electrodes. Moreover, some human friendly electronics including soft biorobotics, active medical devices, wearable electronics, and soft haptic devices will require ultralow voltage high-performance ionic actuators with biocompatible and biodegradable properties. These existing problems inspired us to further develop ultralow voltage high-performance low-priced bioartificial muscles. To overcome these problems, biofriendly ultralow voltage actuated materials are desired. A recent significant step is the discovery of IEAP actuators using naturally biopolymer cellulose.^[11–20] Cellulose is the most abundant polymer in the world, having received great attention because of its low cost, lightweight, biocompatibility, and biodegradability. But the cellulose-based actuators reported already in the open literature still exhibit low actuation performances (maximum bending strain: 0.24%), as shown in Table S2, Supporting Information. Additionally, cellulose contains relatively high non-fibrous substances (hemicellulose and

Prof. F. Wang, Prof. Q. Li
Faculty of Mechanical Engineering and Automation
Zhejiang Sci-Tech University
Hangzhou 310018, China
E-mail: lqchuan@zstu.edu.cn

Prof. J.-O. Park, Prof. E. Choi
Korea Institute of Medical Microrobotics
43-26 Cheomdangwagi-ro, Buk-gu, Gwangju 61011, Republic of Korea
E-mail: jop@jnu.ac.kr; eunpyochoi@jnu.ac.kr

Prof. J.-O. Park, Prof. E. Choi
School of Mechanical Engineering
Chonnam National University
77 Yongbong-ro, Buk-gu, Gwangju 61186, Republic of Korea

Prof. S. Zheng
School of Medical Imaging
Xuzhou Medical University
Xuzhou 221006, China

 The ORCID identification number(s) for the author(s) of this article can be found under <https://doi.org/10.1002/adfm.202007749>.

DOI: 10.1002/adfm.202007749

lignin) that people have to use chemical substances to remove at high temperatures, resulting in a large amount of difficult-treat waste water and serious environmental pollution. These problems hinder the further development and application of cellulose-based actuators. Therefore, the development of novel high-performance cellulose-based actuators with considerable bending strain, fast response time, low actuation voltage, and high durability is highly desirable.

Quite different from other native celluloses, bacterial cellulose (BC) with unique biomacromolecular architecture has a higher biocompatibility and biodegradability, more purity and crystallinity, higher water-holding capacity, stronger mechanical properties, and no lignin or hemicellulose.^[21–23] The existing BC-based actuators displayed low bending strain (0.05%; Table S2, Supporting Information) because of their high mechanical properties, which was attributed to BC having an aggregated-entangled structure. Recently, the functional carboxylated BC (FCBC) fabricated by TEMPO (2,2,6,6-tetramethylpiperidine-1-oxyl radical)-mediated oxidation has received great attention owing to its uniquely individual nanofibers in water, facile membrane formation, increased surface free energy, and excellent cell compatibility.^[24,25] The carboxylate groups are selectively oxidized on surfaces of BC and the homogeneous FCBC dispersion with individual nanofibers in water can be obtained resulting from the strong electrostatic repulsion among negatively charged carboxylate ions. In particular, the carboxylate functional groups in FCBC can act as protonation-active sites, leading to the enhanced ion transport properties. Furthermore, these functional groups allow FCBC to be functionalized with other functional conducting polymers and bioactive ionic liquids (IL). According to these unique properties, although some researchers recently developed TOBC-Graphene-IL ionic actuator (bending strain: 0.13%; response time: ≈ 8 s) and CZ-PL ionic actuator (bending strain: 0.28%; response time: ≈ 30 s), both of which showed better actuation performances than those of BC-based actuators (Table S2, Supporting Information), these designed ionic actuators still demonstrated low bending strain and slow response time compared with other synthetic ionic polymer actuators because of their low porosity, low specific capacitance, low ionic exchangeable capacity, and low ionic conductivity, which inspired us to further develop high-performance durable FCBC-based actuators with superior electro-chemo-mechanical properties.

Among electroactive conducting polymers (ECPs), polypyrrole (PPy) has drawn extensive attention owing to its high conductivity, excellent biocompatibility and biodegradability, high theoretical capacity, good energy density, inherent fast redox switching, and facile synthesis.^[26–28] More interestingly, FCBC with individual nanofibers in water means that pyrrole (Py) can be well dispersed in FCBC nanocomposite network and then uniformly deposited on surfaces of FCBC nanofibers after chemical polymerization. Especially, the presence of abundant carboxylate functional groups on FCBC surfaces can enhance the adsorption process of positively charged PPy nanoparticles in chemical polymerization process, finally resulting in a high porous and conductive structure. To the best of the authors' knowledge, the eco-friendly nanobiocomposite based on FCBC and PPy has not been explored as ionic exchangeable polymer membranes for developing

high-performance bioartificial muscles and further potential bioapplications.

In this study, for the first time, we designed an high-performance ultralow voltage ionic bioartificial muscle based on biofriendly FCBC, PPy nanoparticles, and IL (1-Ethyl-3-methylimidazolium tetrafluoroborate, [EMIM][BF₄]), thereby achieving a large deformable, fast response, and high-durable ionic actuator that can realize potentially bioinspired applications, as shown in **Figure 1**. The highly porous and conductive FCBC-PPy nanocomposite was prepared by the chemical oxidative polymerization of Py on surfaces of FCBC nanofibers in aqueous medium. In particular, the presence of abundant carboxylated groups on FCBC could enhance the adsorption process of highly conductive PPy nanoparticles during the chemical polymerization process, thereby offering additional active sites and resulting in a highly porous and conductive nanostructure. The FCBC-PPy-IL nanobiocomposite membrane was further synthesized by the fast-drying casting of FCBC-PPy with IL. The designed membrane demonstrated a notable promotion of the electrochemical properties, easy and fast charge-transfer responses, and tuned mechanical properties, resulting from its large surface area, high porosity, abundant microporosity and mesoporosity, tuned mechanical properties, and strong ionic interactions among functional carboxylated groups of FCBC, PPy nanoparticles, and IL. These remarkable features facilitated the ion movement within the nanobiocomposite matrix. Finally, the ionic actuator was prepared by depositing the flexible, biofriendly, and conductive polymer poly(3,4-ethylenedioxythiophene)-polystyrenesulfonate (PEDOT:PSS) treated with dimethyl sulfoxide (DMSO) on both sides of the proposed membrane. The addition of DMSO could lead a decrease in the PPS content at surfaces of PEDOT grains, thereby weakening the barrier effect and eventually resulting in improved ion migration and charge transport within electrodes. Notably, the newly designed FCBC-PPy-IL ionic soft actuator exhibited larger bending strain and faster response time under ultralow input voltage than those of pure FCBC-IL actuator, which was mainly attributed to the combined contribution of large ion-accessible surface area, excellent electron donor-acceptor interactions, and high charge storage ability of the proposed membrane and electrode layers. More importantly, we successfully demonstrated promising bioinspired applications including the grapple robot, bionic medical stent, bionic flower, and wings-vibrating using FCBC-PPy-IL actuators. The designed ionic soft actuator based on ionically crosslinked PPy-coated FCBC and its bioinspired robotic designs will provide an available pathway for boosting the development of bioartificial muscles, as well as next-generation soft robotics and active medical devices.

2. Results and Discussion

2.1. Structure and Chemical Characterization of Ionically Cross-Linked FCBC-PPy-IL

The synthesis of FCBC-PPy-IL was carried out by dry-casting FCBC-PPy dispersions with IL on a petri dish. Briefly, the

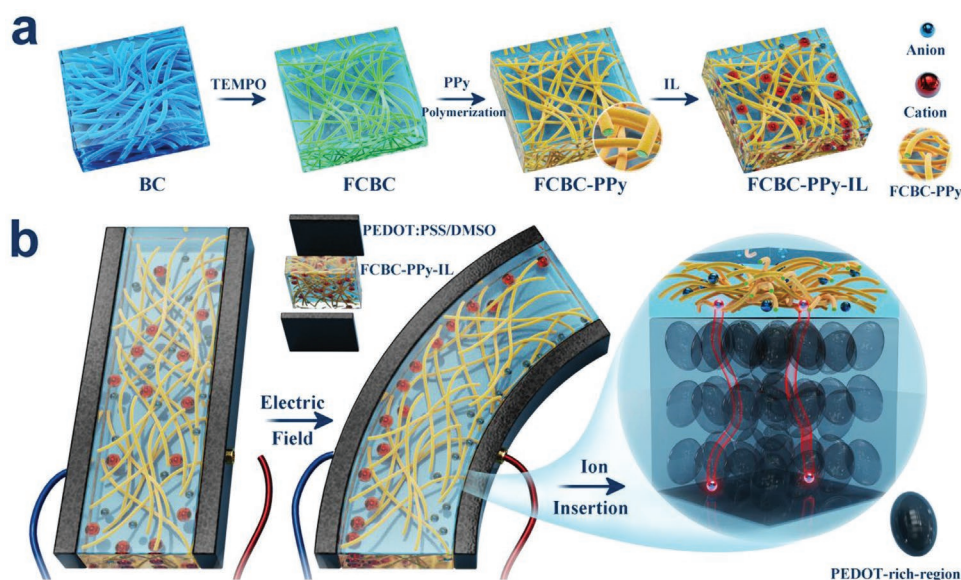


Figure 1. Schematic diagrams for the synthetic route of FCBC-PPy-IL ionically crosslinked nanocomposites and the actuation mechanism of the designed novel ionic bioartificial muscle based on PEDOT:PSS/DMSO electrodes. a) Synthesis steps of FCBC-PPy-IL ionically crosslinked nanobio-composites. b) The actuation mechanism of the ionic bioartificial muscle with PEDOT:PSS/DMSO electrodes showing large bending strain and fast response time under an ultralow input voltage due to its large ion-accessible surface area, excellent electron donor-acceptor interactions, and high charge storage ability.

homogenous FCBC dispersions with individual nanofibers were fabricated by the oxidation of original BC using TEMPO-mediated oxidation method (Figure S1, Supporting Information).^[29,30] The Fourier transform infrared spectroscopy (FT-IR) results proved that significant amounts of functional C6 carboxylated groups were selectively formed on each surface of BC nanofibers (Figure S2, Supporting Information). The FCBC-PPy dispersions were fabricated through the chemical oxidative polymerization method, where FCBC nanofibers and iron (III) chloride (FeCl_3) acted as the template and oxidant, respectively.^[31,32] FCBC with individual nanofibers in water allows the successful and homogeneous deposition of PPy nanoparticles on surfaces of FCBC nanofibers (Figure S2, Supporting Information). The proposed FCBC-PPy showed a high conductivity ($\approx 6.63 \text{ S cm}^{-1}$), which was mainly due to the presence of functional carboxylated groups on FCBC nanofibers boosting the adsorption of PPy nanoparticles during the chemical oxidative polymerization. This is because the functional carboxylated groups were able to act as counter ions for the positively charged PPy nanoparticles. The eco-friendly FCBC-PPy-IL nanobiocomposite membrane was further synthesized via the rapid-drying solution casting of FCBC-PPy with IL ($[\text{EMIM}][\text{BF}_4]$). The characteristic bands including the O–H stretching vibration and the ether C–O–C bonding became relatively stronger, exhibiting strong ionic interactions among the functional carboxylated groups of FCBC, PPy nanoparticles, and ILs, as depicted in Figure S3, Supporting Information. The spectra of the FCBC-PPy-IL membrane displayed at 3343 cm^{-1} (O–H stretching), 3165 and 3119 cm^{-1} (C–H of imidazole ring stretching vibration), 1565 cm^{-1} (C=O stretching), 1455 cm^{-1} (C=N stretching), 1314 cm^{-1} (C–N stretching), 1169 cm^{-1} (N–H stretching), 1015 cm^{-1} (C–O stretching), 845 and 752 cm^{-1} (BF_4^- groups), respectively. Obviously, the intensity of the characteristic peak

at 1565 cm^{-1} band (C=O stretching) was enhanced in comparison with FCBC-PPy, indicating strong interactions between functional carboxylated groups of FCBC and IL. The characteristic peaks appeared at 3165 and 3119 cm^{-1} , 845 and 752 cm^{-1} corresponding to C–H and BF_4^- groups of IL ($[\text{EMIM}][\text{BF}_4^-]$), further confirming the ionic interactions between FCBC and IL. Importantly, the increased intensity at 1169 cm^{-1} (N–H stretching) was because of the strong ionic interactions between PPy and IL. Thus, these FT-IR analyses results clearly validate the strong ionic interactions among FCBC, PPy, and IL.

The morphologies of pure FCBC, FCBC-PPy, and FCBC-PPy-IL nanobiomembranes were investigated by employing field emission electron microscope (FESEM), transmission electron microscope (TEM), and atomic force microscope (AFM), confirming that PPy nanoparticles were uniformly coated on surfaces of FCBC nanofibers and that the highly conductive FCBC-PPy nanocomposite fibers were effectively and strongly bound with IL (Figure 2a–l). These unique structural morphologies were mainly attributed to the strong ionic interactions among the functional carboxylated groups on surfaces of FCBC nanofibers, PPy nanoparticles, and IL. The FCBC membrane has a fibrous structure consisting of ultrafine nanofibers (Figure 2a); after the chemical polymerization, the PPy nanoparticles were successfully and homogeneously deposited on FCBC individual nanofibers, creating additional continuous conductive pathways (Figure 2b). This was mainly owing to the presence of abundant functional carboxylated groups on FCBC surfaces that could enhance the adsorption of the positively charged PPy nanoparticles during the chemical oxidative polymerization.^[33] These findings resulted in improved electrochemical properties including a much higher ionic uptake ratio, larger ionic conductivity, and higher ion exchange capacity

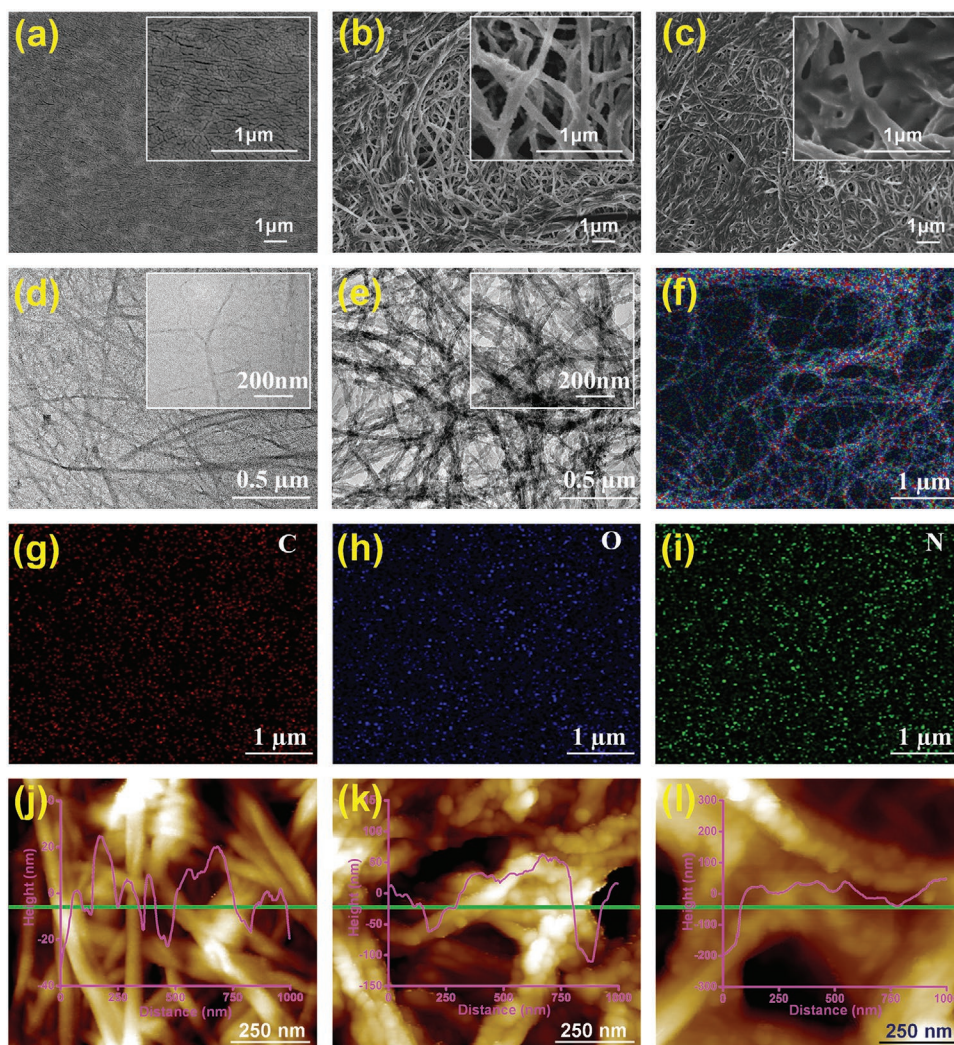


Figure 2. Morphological characterizations of the FCBC-PPy-IL nanobiocomposite membranes. FESEM images of a) FCBC, b) FCBC-PPy, and c) FCBC-PPy-IL. TEM images of d) FCBC and e) FCBC-PPy. f) The elemental mapping image of FCBC-PPy and its corresponding g) carbon, h) oxygen, and i) nitrogen elemental mapping images. AFM images of j) FCBC, k) FCBC-PPy, and l) FCBC-PPy-IL.

than those of pure FCBC (Table S3, Supporting Information). The corresponding values were calculated to be 121.53%, $3.52 \times 10^{-3} \text{ s cm}^{-1}$, 2.25 meq. g^{-1} , which were 3.98, 2.41, and 1.24 times larger than those of pure FCBC, respectively. The highly conductive and porous nanocomposite structure of the FCBC-PPy facilitated ion migration and shortened the ion diffusion distance from the internal electrolyte to the electrode layers. The surface images of the FCBC-PPy-IL nanocomposite revealed an ionically cross-linked network structure consisting of highly porous FCBC-PPy nanocomposite fibers and well-embedded IL (Figure 2c). The structural morphology was because of the strong ionic interactions among functional carboxylated groups of FCBC, PPy nanoparticles, and IL. Furthermore, the TEM (Figure 2d–i; Figure S4, Supporting Information) and AFM (Figure 2j–l; Figure S5, Supporting Information) images furtherly demonstrated that PPy nanoparticles were successfully and homogeneously deposited on FCBC nanofibers and that the FCBC-PPy nanocomposite fibers were effectively and strongly crosslinked with IL.

The structure characterizations of the FCBC-PPy-IL nanobiocomposite membranes were evaluated using N_2 adsorption-desorption isotherms, pore size distributions, X-ray photo-electron spectroscopy (XPS), a thermogravimetric analyzer (TGA), and a high resolution X-ray diffractometer (XRD), providing additional evidence for the formation of highly porous-conductive FCBC-PPy nanocomposite fibers and ionically cross-linked FCBC-PPy-IL nanobiocomposite membrane (Figure 3a–e; Figure S6, Supporting Information). Figure 3a shows a typical N_2 adsorption-desorption isotherm curve for the FCBC-PPy nanocomposite. In the case of FCBC, the surface area and pore volume were $3.29 \text{ m}^2 \text{ g}^{-1}$ and $0.01 \text{ cm}^3 \text{ g}^{-1}$, respectively; however, for the FCBC-PPy nanocomposite, the corresponding values were $101.73 \text{ m}^2 \text{ g}^{-1}$ and $0.48 \text{ cm}^3 \text{ g}^{-1}$. The enhanced surface area and pore volume obviously proved that massive PPy nanoparticles were successfully coated on surfaces of FCBC-PPy nanofibers. More importantly, the nitrogen uptake under relatively low pressure ($P/P_0 < 0.3$) indicated the existence of massive micropores in FCBC-PPy nanocomposites.

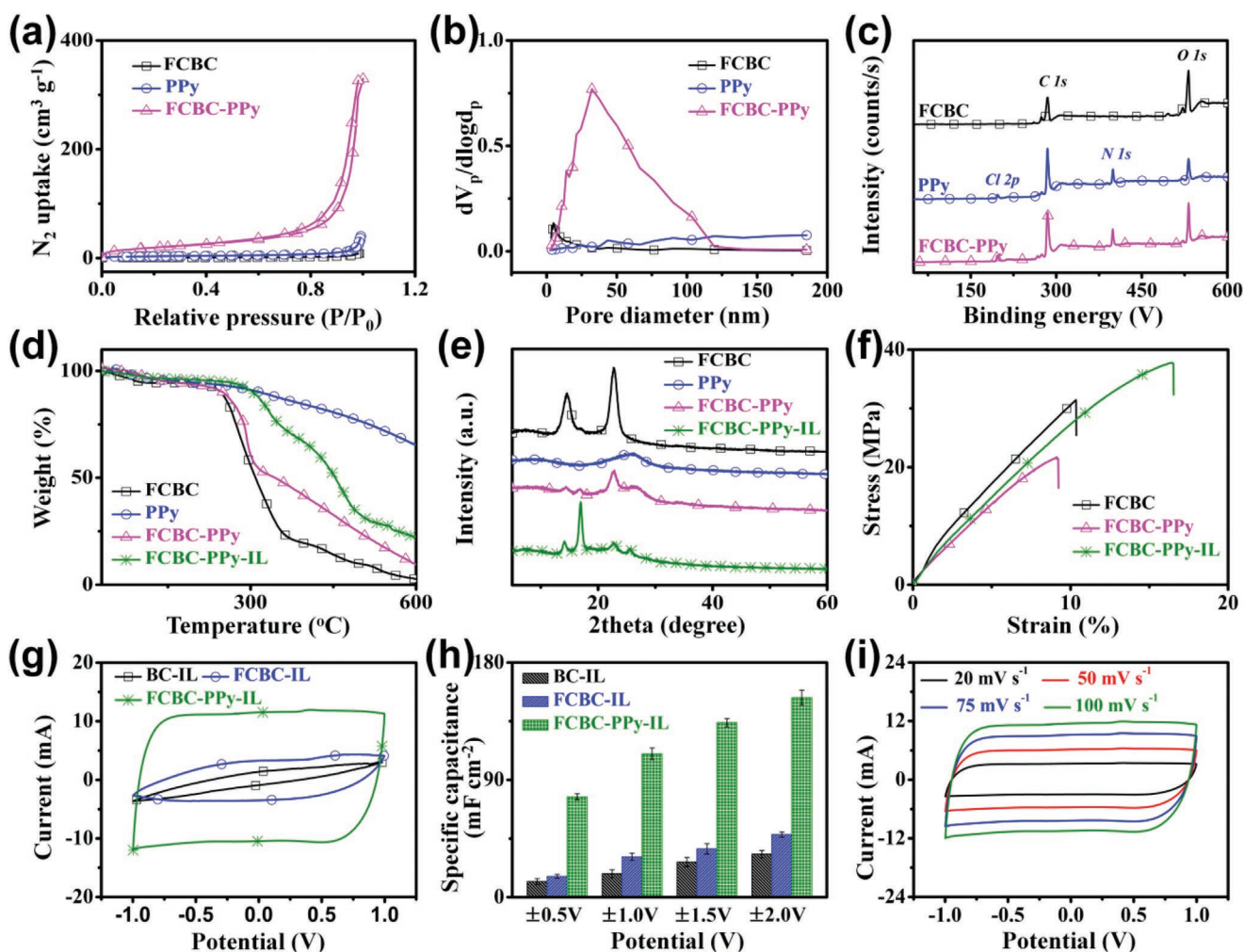


Figure 3. Characterization of FCBC-PPy-IL. a) N_2 adsorption-desorption isotherms and b) the corresponding pore-size distributions of FCBC, PPy, and FCBC-PPy. c) High-resolution XPS spectra. d) TGA curves, e) XRD curves, and f) Stress-strain curves of FCBC, FCBC-PPy, and FCBC-PPy-IL. g) CV curves of the BC-IL, FCBC-IL, and FCBC-PPy-IL actuators based on PEDOT:PSS/DMSO electrodes under a scan rate of 100 mV s^{-1} in the potential window of $+1.0$ to -1.0 V. h) Specific capacitance values of the actuators under a scan rate of 100 mV s^{-1} in various potential windows. i) CV curves of the FCBC-PPy-IL actuator under various scan rates in the potential window of -1.0 to 1.0 V.

There was a sharp nitrogen uptake at the relatively high pressure approaching 1, demonstrating the existence of abundant meso- and macropores.^[34] The large surface area and high pore volume of FCBC-PPy nanocomposite facilitated ion migration within electrolyte membranes. The pore size distribution centered at 27.65 nm for the FCBC-PPy, while the corresponding value of pure FCBC occurred at 4.83 nm (Figure 3b), exhibiting the successful deposition of homogenous PPy nanoparticles on FCBC nanofiber surfaces. These findings reveal that the FCBC-PPy nanocomposite with a highly porous and conductive structure is expected to be an excellent ionic polymer membrane candidate for high-performance ionic artificial muscles. Furthermore, XPS was conducted to evaluate the chemical binding state and composition of the FCBC-PPy nanocomposites. The XPS curves (Figure 3c) and element analysis (Figure S6, Supporting Information) confirmed the successful incorporation of PPy nanoparticles on surfaces of FCBC nanofibers. For pure PPy, two main peaks displayed at 285 and 399.5 eV belonged to C 1s and N 1s;^[35] however, the corresponding FCBC-PPy

nanocomposite value decreased to 284.5 and 399 eV, respectively. This was due to the strong interactions between $-\text{COOH}$ groups of FCBC and $-\text{N}-\text{H}$ in the PPy ring; the abundant anions (COO^-) could act as counter ions for the positively charged nitrogens of PPy.^[33]

We further explored the thermal stability of the FCBC-PPy-IL nanobiomembrane by using TGA analysis, demonstrating the strong ionic interactions among functional carboxylated groups of FCBC, IL, and PPy nanoparticles (Figure 3d). The TGA curve of pure FCBC showed three decomposition stages. The first step at $30\text{--}220^\circ\text{C}$ was attributed to the evaporation of water; the second stage displayed at around $220\text{--}335^\circ\text{C}$ because of the side-chain degradation of the FCBC polymer; the third step corresponded to the elimination of residual compounds at $335\text{--}600^\circ\text{C}$. Notably, we observed that the FCBC-PPy nanocomposite exhibited higher thermal stability than that of pure FCBC, which was as a result of PPy nanoparticles that successfully adhered to FCBC nanofibers. Importantly, the thermal stability of the FCBC-PPy-IL membrane was improved by the

addition of IL, benefiting from the strong ionic interactions and interfacial interactions among FCBC, PPy, and IL, which in turn offered thermal processing advantages. Additionally, XRD patterns of the FCBC-PPy-IL membrane further proved the existence of strong ionic interactions within the designed membrane matrix (Figure 3e). The pure FCBC exhibited main peaks at around 14.87, 16.71, and 22.69° corresponding to the (1 1 0), (1 1 0), and (2 0 0) planes of polymorph cellulose.^[36] Compared with pure FCBC, the FCBC-PPy nanocomposites showed one new characteristic peaks at around 26.07°, resulting from the successful incorporation of PPy nanoparticles to FCBC nanofiber surfaces. However, after the addition of IL, the FCBC-PPy-IL nanocomposite membrane exhibited the relatively high intensities at around 14.08°, 16.94°, and a relatively low intensity at 22.69°, which were attributed to the strong ionic interactions and interfacial interactions within the membrane matrix. These observations clearly demonstrated the successful coating of PPy nanoparticles on surfaces of FCBC nanofibers and strong ionic interactions among FCBC, PPy, and IL. The mechanical properties of the nanobiocomposite membranes were evaluated by using the tensile test. Figure 3f shows typical stress-strain curves of the FCBC-PPy-IL membrane, and the calculated values of mechanical properties are shown in Table S3, Supporting Information. Appreciably, the tensile strength and Young's modulus decreased from pure FCBC (31.73 MPa and 0.44 GPa) to FCBC-PPy nanocomposites (21.69 MPa and 0.31 GPa). Also, the elongation at break of FCBC-PPy (9.12%) was much lower than that of pure FCBC (10.56%). The decrease in the mechanical properties resulted from the weakened intra- and intermolecular hydrogen bonding of FCBC nanofibers, which was caused by the incorporation of PPy nanoparticles. However, the FCBC-PPy-IL exhibited higher tensile strength and Young's modulus (37.76 MPa and 0.38 GPa) and elongation at break (16.39%) in comparison with FCBC-PPy, mainly ascribed to the strong ionic interactions and interfacial interactions among FCBC, PPy, and IL. More interestingly, the larger surface area and micro and mesoporosity of the membrane facilitated the ionic and interfacial interactions, which eventually resulted in enhanced mechanical properties.

As electrochemical properties of ionic actuators are the crucial factors in evaluating actuation performances, cyclic voltammetry (CV) tests of the FCBC-PPy-IL ionic actuator based on PEDOT/DMSO electrodes were done in a two-electrode system. Figure 3g shows CV curves of the FCBC-PPy-IL actuator under a scan rate of 100 mV s⁻¹ in the voltage range of +1.0 to -1.0 V. Notably, the FCBC-PPy-IL actuator exhibited a rectangular-like CV curve, indicating the ideal electrical double-layer capacitor behavior. The area under the CV curve is much larger for the actuator in comparison with pure FCBC-IL actuator. Importantly, the FCBC-PPy-IL actuator exhibited a higher specific capacitance (113.7 mF cm⁻²) than those of the FCBC-IL and BC-IL actuators (31.5 and 18.1 mF cm⁻²) under a scan rate of 100 mV s⁻¹ in the potential window of +1.0 to -1.0 V. The corresponding specific capacitance values were also significantly larger under various potential windows compared to those of the FCBC-IL and BC-IL actuators (Figure 3h). The CV curves of the actuator under various scan rates (20–100 mV s⁻¹) also displayed unaltered shapes at all scan rates (Figure 3i). The variations of specific capacitances with different scan rates of

the actuator are shown in Figure S7, Supporting Information, exhibiting that the FCBC-PPy-IL actuator possessed significantly higher specific capacitances than the other two actuators. The excellent CV responses and the enhanced specific capacitance of the designed actuator were mainly ascribed to its large surface area, high porosity, and strong ionic interactions, which not only facilitated easy and fast ion transport inside the membrane matrix but also improved the efficient binding interaction. Additionally, the presence of abundant functional carboxylated groups on FCBC could promote the adsorption of high and conductive PPy nanoparticles, which led to extra active sites and resulted in the improvement of the charge transport and current density.

2.2. Actuation Performances of FCBC-PPy-IL Bioartificial Muscles

To evaluate actuation performances of the designed FCBC-PPy-IL ionic bioartificial muscles, various electrical inputs were applied to the PEDOT:PSS treated with DMSO electrode layers (Figure 4a–h; Figure S8, Supporting Information). Figure 4a shows the bending displacement of the BC-IL, FCBC-IL, and FCBC-PPy-IL actuator under a low sinusoidal voltage (± 0.5 V) at a frequency of 0.1 Hz. Evidently, the peak bending displacement of the FCBC-PPy-IL actuator was about ± 6.9 mm, which was 4.6 and 9.8 times more than those of the FCBC-IL (± 1.5 mm) and BC-IL actuators (± 0.7 mm), respectively. Remarkably, the proposed actuator demonstrated better bending displacement and faster response time than the FCBC-IL and BC-IL actuator, which were mainly attributed to its high surface area, large porosity, high specific capacitance, and enhanced electrochemical properties, not only promoting ion migration within the membrane but also facilitating the efficient binding interaction with electrodes. The enhanced electrochemo-mechanical properties resulted from the combined contribution of highly conductive PPy nanoparticles uniformly coated on surfaces of FCBC nanofibers and the strong ionic interactions among FCBC, PPy, and ILs. The FCBC(1.3)-PPy-IL actuator shows larger bending deformation than that of the FCBC(0.9)-PPy-IL actuator, displaying that the functional carboxylated groups in the BC can affect actuation performances of the ionic actuators (Figure S9, Supporting Information). The current response of the actuator was investigated under a sinusoidal voltage (± 0.5 V) at a frequency of 0.1 Hz, and the peak current was up to 7.1 mA (Figure S10, Supporting Information). Figure 4b displays the peak-to-peak bending displacement of all ionic actuators at a functional frequency under sinusoidal input of ± 0.5 V. As the applied frequency increased, the peak displacement of the actuator gradually decreased for all ionic actuators owing to insufficient time for the movement of IL within the porous membrane toward electrode layers. However, the FCBC-PPy-IL actuator still exhibited a stable frequency response and showed the maximum bending displacement for all applied frequencies due to the excellent electro-chemical properties of ionically crosslinked FCBC-PPy-IL nanocomposites, such as a highly porous flexible structure, excellent ionic transportation, and high specific capacitance. Moreover, we investigated the bending displacements of all actuators under

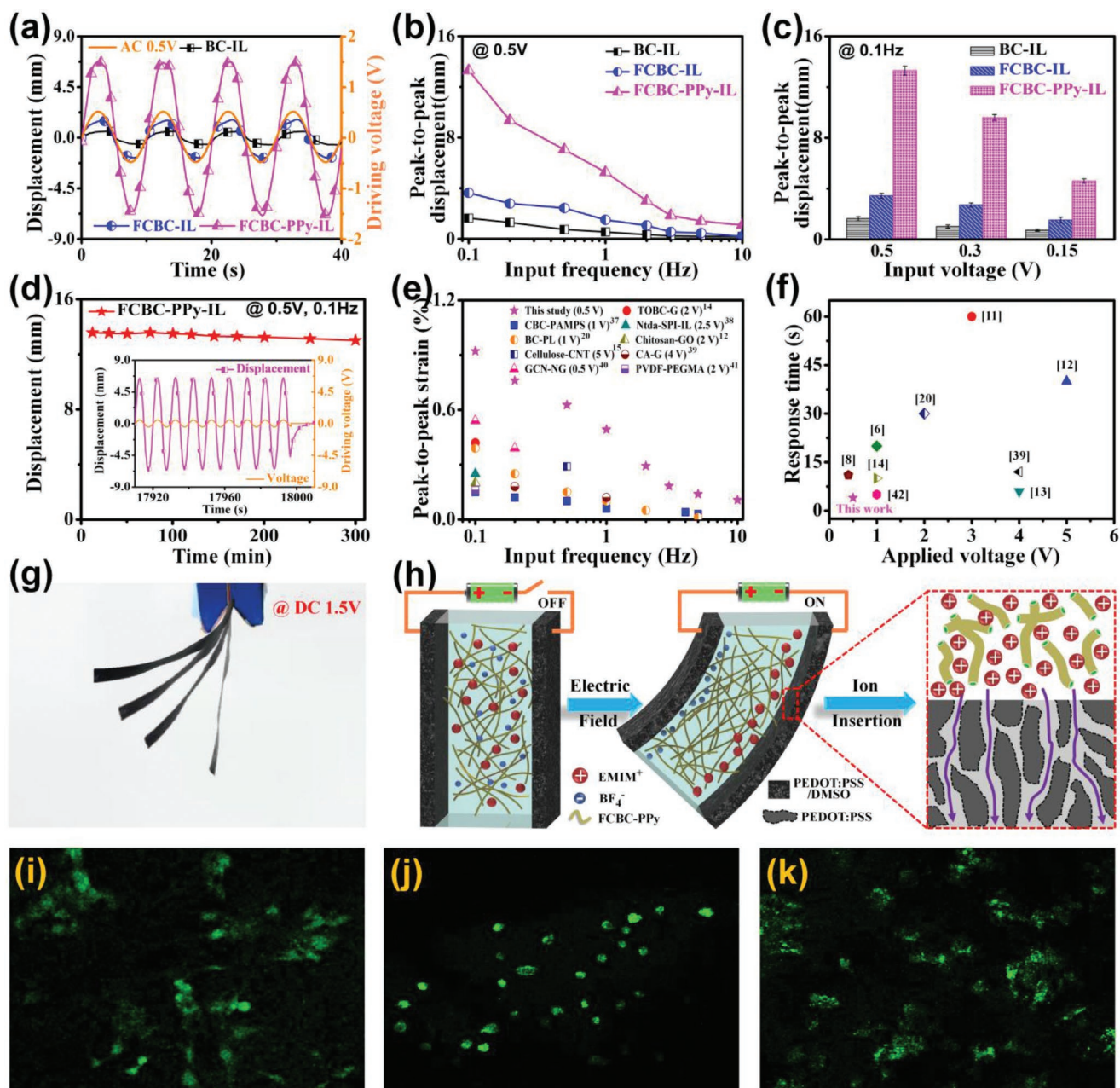


Figure 4. Actuation performances of the FCBC-PPy-IL actuators. a) Peak-to-peak displacements of the actuators under a sinusoidal input voltage of ± 0.5 V at 0.1 Hz. b) Peak-to-peak displacements of the actuators at a range of frequencies from 0.1 to 10 Hz under a sinusoidal input voltage of ± 0.5 V at 0.1 Hz. c) Variation of peak-peak displacements of the actuators with different input voltages (0.15–0.5 V) at 0.1 Hz. d) Actuation durability test of the actuator under a sinusoidal input voltage of ± 0.5 V at 0.1 Hz. Comparison of e) bending strains and f) response times of the designed actuator with those of the reported soft ionic actuators. g) Electromechanically deformed shapes of the actuator under a step excitation of 1.5 V. h) Schematic diagram of an actuation mechanism. Confocal images of live cells attachments for g) FCBC, h) FCBC-PPy, and i) FCBC-PPy-IL actuators.

various sinusoidal input voltages. As depicted in Figure 4c, the bending displacements of all ionic actuators increased as the applied voltage input increased. Surprisingly, the actuator still showed relatively large peak-to-peak displacement (4.5 mm) under an ultralow input voltage (± 0.15 V). The peak-to-peak bending displacements of ionic actuators were also evaluated under a triangle wave voltage (± 0.5 V) at a frequency of 0.1 Hz (Figure S11, Supporting Information). Similar to the findings for the sinusoidal output response, the actuator exhibited sim-

ilar trend of bending responses. These results demonstrate that the newly proposed actuator can perform effectively at ultralow input voltages.

Furthermore, the bending displacements of all ionic actuators were investigated under an applied DC voltage of 0.5 V (Figure S12, Supporting Information). The maximum displacements of the FCBC-PPy-IL, FCBC-IL, and BC-IL actuators were 8.1, 1.9, and 0.8 mm, respectively. Noticeably, the FCBC-PPy-IL actuator showed better bending displacement and

faster response time compared with other two ionic actuators. More importantly, the actuator did not exhibit the back-relaxation phenomenon, which was mainly due to the weakly polar carboxylate groups on surfaces of FCBC nanofibers, easy-fast ionic transportation, and the strong ionic interactions among FCBC, PPy, and IL. Ultimately, for practical applications including soft robotics, biomedical devices, and wearable devices, ionic soft actuators are required to possess not only large bending deformation but also excellent actuation durability. Therefore, the retention actuation performance was performed for 5 h under a continuous sinusoidal input voltage of ± 0.5 V at a frequency of 0.1 Hz, as seen in Figure 4d. Strikingly, the FCBC-PPy-IL actuator displayed excellent actuation durability without an apparent displacement degradation and response distortion. After an actuation bending test for 5 h, the peak displacement of the actuator still retained about 96% of its highest peak displacement. These findings reveal that the proposed actuator can provide a constant conductive path for ion migration and charge transfer in long-duration functioning.

According to the above results, the designed FCBC-PPy-IL ionic actuator presented remarkably large bending strain (0.93%) under a sinusoidal voltage (± 0.5 V) at a frequency of 0.1 Hz compared with the maximum bending strains of other ionic soft actuators, as reported in the recent literature on PVDF-based ionic actuators (0.52% under 2.5 V at 0.1 Hz), nafion-based ionic actuators (0.68% under 1.0 V at 0.1 Hz), and cellulose-based ionic actuators (0.28% under 1.0 V at 0.1 Hz) (Figure 4e; Table S1, S2, Supporting Information).^[12,13,15,20,37–41] Also, we found the ionic soft actuator demonstrated relatively faster response time (≈ 4 s) in comparison to other ionic actuators (Figure 4f; Table S1, S2, Supporting Information).^[6,8,11–14,20,39,42] Moreover, the maximum energy density was as high as 6.81 kJ m^{-3} (Figure S13, Supporting Information), and the maximum power density was 5.11 kW m^{-3} (Figure S14, Supporting Information), which almost reach the capability of human skeletal muscles.^[9] The excellent actuation performance of the FCBC-PPy-IL actuator was mainly attributed to its high porosity, large specific capacitance, tuned mechanical properties, and strong ionic interactions among FCBC, PPy, and IL. Another reason for the enhanced actuation performance was that the PEDOT:PSS/DMSO composite electrodes with large conducting area and improved ionic transportation were well coated on surfaces of the proposed membrane (Figure S15, Supporting Information). In particular, the PEDOT:PSS polymer is usually arranged in grains with a highly conductive PEDOT-rich core and an insulating PSS-rich shell, which acts as a passive barrier for charge transport. The grain sizes increase owing to the addition of DMSO (Figure S16, Supporting Information), leading to increased membrane roughness (Figure S17, Supporting Information). This caused a reduction in the contact surface between the grains, resulting in enhanced charge transport within electrodes. Also, the addition of DMSO to PEDOT:PSS triggered a decrease in the PSS content at surfaces of PEDOT grains, indicating the PEDOT:PSS electrodes treated with DMSO have larger conducting areas and enhanced ionic transportation as a consequence of the reduction in the charge-transport barriers and the enlargement of the conducting PEDOT-rich cores.^[43,44] Furthermore, the formation of

PEDOT:PSS doped DMSO was furtherly confirmed by FT-IR (Figure S18, Supporting Information) and energy-dispersive X-ray spectroscopy measurements (Figure S19, Supporting Information). Additionally, the blocking force of the actuators was measured under a DC voltage of 0.5 V, displaying much larger than those of the FCBC-IL and BC-IL actuators (Figure S20, Supporting Information). Moreover, Figure 4g exhibits largely deformed shapes of the proposed actuator under a DC voltage of 1.5 V (Movie S1, Supporting Information). Ultimately, Figure 4h presents the schematic illustration of the actuation mechanism for the designed FCBC-PPy-IL actuator. When an electrical field was applied to PEDOT:PSS electrodes, the larger molecule size cations (EMIM^+) and smaller anions (BF_4^-) inside the membrane migrated to cathode and anode sides, respectively. The accumulation of cations and anions near electrode sides induced a relative volume difference, leading to a mechanical bending deformation toward the anode. The cations and anions moved into electrode layers and caused the electrochemical doping process of PEDOT:PSS layers, resulting in the improved bending deformation. Thus, the actuation mechanism of the actuator was attributed to the synergistic effects of the migration of ILs with larger cations and smaller anions in the electrolyte membrane and the electrochemical doping process of the PEDOT:PSS electrode layers under an electrical field.

More interestingly, the biocompatibility of the FCBC-PPy-IL actuator was investigated using confocal image analysis (Figure 3i–k). The NIH/3T3 mouse fibroblast cells were seeded on the three sterilized membranes at a density of 2×10^4 cells/cm². Then, the cells were incubated overnight in 37 °C in a humidified 5% CO₂ atmosphere to allow cell attachment on surfaces of three membranes. Subsequently, the NIH/3T3 cells were stained with the cell proliferation assay kit (green fluorescence) for living cells labeling following the standard protocol. Then the NIH/3T3 cells were washed carefully with cold PBS to remove the unattached cells, fixed with 4% paraformaldehyde solution. The attachment of NIH/3T3 cells on the membranes were observed by a confocal laser scanning microscopy. As shown Figure 3i–k, the NIH/3T3 cells exhibited excellent attachments on the three ionic actuators after overnight co-incubation. Besides, for the FCBC actuator, the healthy living condition and normal morphology of NIH/3T3 cells could be clearly observed from green fluorescence signal, indicating the excellent biocompatibility of the FCBC actuator. Evidently, there was almost no effect on the cell attachments and viability of the FCBC after the deposition of PPy nanoparticles and subsequent cross-linking with IL. These results confirmed the excellent biocompatibility of the proposed FCBC-PPy-IL actuator, unveiling its further applications in the biomedical fields.

To determine the potential applications according to the large actuation bending strain and excellent biocompatibility, we focused on the proof of concept where various soft robotics were developed using FCBC-PPy-IL-based actuators (Figure 5a–d). The proposed actuators were first employed to make a grapple robot for manipulating objects (Figure 5a; Movie S2, Supporting Information). We found that the grapple robot could quickly grasp, lift, transport, and release one object (weight: 80 mg). The grapple robot was placed on top of the object, and approached

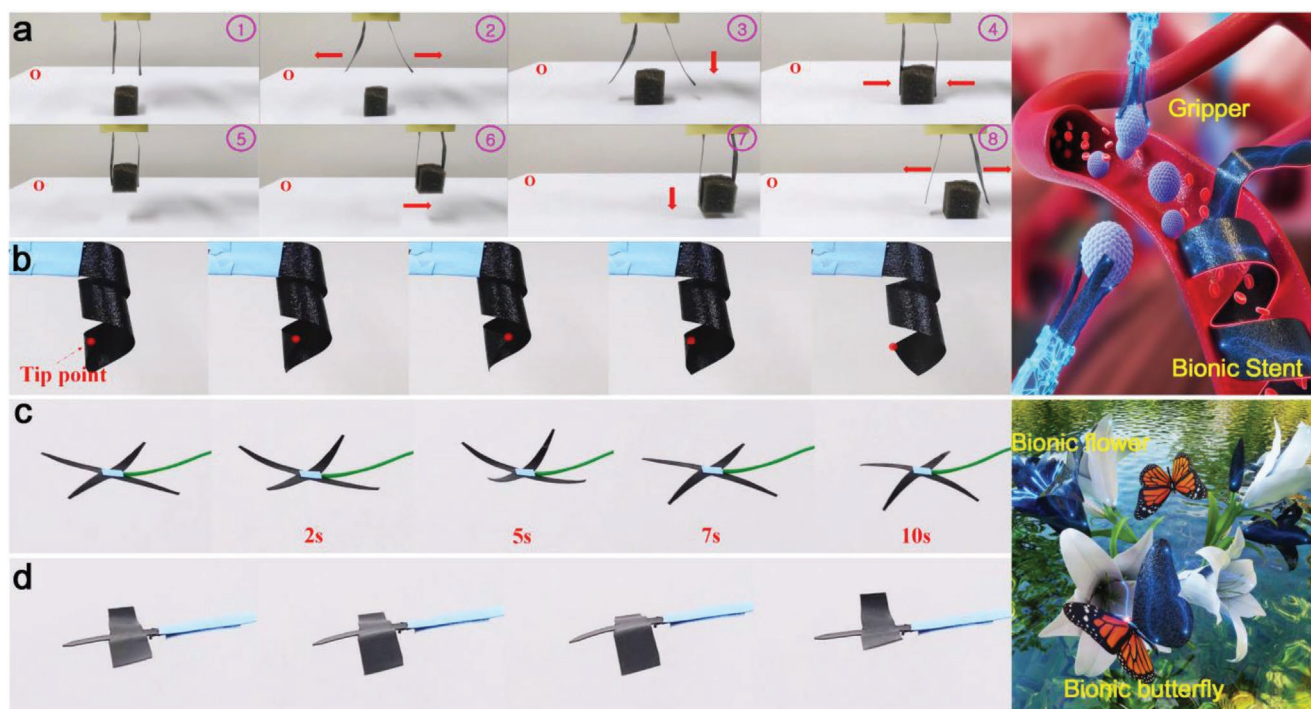


Figure 5. Bioinspired applications of the FCBC-PPy-IL actuators. a) Operation of the grapple robot consisting of two actuators under an input voltage of 1.0 V. The weight of the relocated plastic foam was 80 mg. b) Optical images of a bionic medical stent. At first, the stent was in a static position. Thereafter, the stent would contract and then expand after applying a square input of 1.0 V at 0.1 Hz. c) Bionic flower to mimic folding and blooming process under a square input of 1.0 V at 0.1 Hz. d) Optical images of a flying robot prototype with different wing positions. Initially, the flying robot prototype was in dead position; after applying an AC input of 1.5 V at 0.1 Hz, the behavior of the bionic bird was similar to that of a live butterfly.

it. The bionic arms were actuated and they grasped the object when an input voltage of 1.0 V was applied. Subsequently, the grapple robot moved to the target position and released the object. Furthermore, the grapple robot could successfully grasp and move two objects (Figure S22 and Movie S3, Supporting Information), whose weight (140 mg) was 4.67 times greater than that of our previous report.^[37] More importantly, a bionic medical stent using a helical FCBC-PPy-IL actuator was designed (Figure 5b; Movie S4, Supporting Information). The radius of the bionic medical stent could be controlled using the proper applied voltage and frequency for biomedical smart systems. As an interesting application, a bionic flower with four petals was designed and fabricated to imitate the petal opening and closing process of the flower, which was cut from a FCBC-PPy-IL actuator. The top and bottom surface was connected to the cathode and anode, respectively. When a square input voltage of 1 V was applied, the bionic flower's motion was similar to that of the flower *Dionaea muscipula* (Figure 5c; Movie S5, Supporting Information). The bionic flower could change from the opening state to the closing state within 5 s, and reversibly return to the opening state in a short time. In addition, a flying robot that mimicked the wing vibration of a butterfly has been constructed (Figure 5d; Movie S6, Supporting Information). Therefore, the newly designed ultralow voltage high-performance FCBC-PPy-IL actuator will have great potential in the fields of bioartificial muscles, bioinspired robotics, active biomedical devices, and wearable electronics.

3. Conclusion

In summary, we report a novel ultralow voltage high-performance ionic bioartificial muscle based on biofriendly FCBC, PPy, and IL. The FCBC-PPy-IL nanobiocomposite membrane was synthesized by doping IL into the FCBC-PPy fabricated using the chemical oxidative polymerization, exhibiting large ion-accessible surface area, excellent electron donor-acceptor interactions, high charge storage ability, and easy-fast ion movement within the membrane matrix. These characteristics were mainly attributed to the abundant micro and mesoporosity, high surface area and porosity, and strong ionic interactions among functional carboxylated groups of FCBC, PPy nanoparticles, and IL. The designed FCBC-PPy-IL ionic bioartificial muscle based on PEDOT:PSS-DMSO electrodes demonstrated astonishing actuation performances, including a large bending strain of 0.93%, broad frequency bandwidth (up to 10 Hz), long actuation durability (retention about 96% for 5 h) under ultralow harmonic input of 0.5 V, and excellent biocompatibility. By exploiting these remarkable features, various soft robotics such as the grapple robot, bionic medical stent, bionic flower, and wings-vibrating, have been realized. Therefore, we anticipate that the FCBC-based bioartificial muscle and its soft robotic designs will promote advancing of the next-generation ecofriendly artificial muscles and guide the process toward the realization of promising applications in soft robotics, wearable devices, and active biomedical electronics including the active stent, cell manipulation, and disease diagnosis.

4. Experimental Section

The detailed experimental process is available in the Supporting Information.

Supporting Information

Supporting Information is available from the Wiley Online Library or from the author.

Acknowledgements

This work is supported by National Natural Science Foundation of China (Grant No. 51905487 and 51525504) and Natural Science Foundation of Zhejiang Province (Grant No. LY21E050023). Moreover, this research was supported by a grant from the Korea Health Technology R&D Project through the Korea Health Industry Development Institute (KHIDI), funded by the Ministry of Health and Welfare, Republic of Korea (grant number HI19C0642). Also, this work is supported by the Science Foundation of Zhejiang Sci-Tech University (ZSTU) under Grant No. 18022220-Y.

Conflict of Interest

The authors declare no conflict of interest.

Keywords

bioartificial muscles, carboxylated bacterial cellulose, ionic actuators, soft robotics

Received: September 11, 2020

Revised: October 29, 2020

Published online: December 11, 2020

- [1] R. H. Baughman, C. Cui, A. A. Zakhidov, Z. Iqbal, J. N. Barisci, G. M. Spinks, G. G. Wallace, A. Mazzoldi, D. D. Rossi, A. G. Rinzler, O. Jaschinski, S. Roth, M. Kertesz, *Science* **1999**, 284, 1340.
- [2] C. Jo, D. Pugal, I. K. Oh, K. J. Kim, K. Asaka, *Prog. Polym. Sci.* **2013**, 38, 1037.
- [3] M. Fuchiwaki, J. G. Martinez, T. F. Otero, *Adv. Funct. Mater.* **2015**, 25, 1535.
- [4] M. Acerce, E. K. Akdogan, M. Chhowalla, *Nature* **2017**, 549, 370.
- [5] S. M. Mirvakili, I. W. Hunter, *Adv. Mater.* **2017**, 30, 1704407.
- [6] G. Wu, X. Wu, Y. Xu, H. Cheng, J. Meng, Q. Yu, X. Shi, K. Zhang, W. Chen, S. Chen, *Adv. Mater.* **2019**, 31, 1806492.
- [7] C. Lu, Y. Yang, J. Wang, R. Fu, X. Zhao, L. Zhao, Y. Ming, Y. Hu, H. Lin, X. Tao, Y. Li, W. Chen, *Nat. Commun.* **2018**, 9, 752.
- [8] M. T. Manzoor, V. H. Nguyen, S. Umrao, J. H. Kim, R. Tabassian, J. E. Kim, I. K. Oh, *Adv. Funct. Mater.* **2019**, 29, 1905454.
- [9] J. Li, W. Ma, L. Song, Z. Niu, L. Cai, Q. Zeng, Z. Zhang, H. Dong, D. Zhao, W. Zhou, S. Xie, *Nano Lett.* **2011**, 11, 4636.
- [10] S. Ma, Y. Zheng, Y. Liang, L. Ren, W. Tian, L. Ren, *Adv. Funct. Mater.* **2020**, 30, 1908508.
- [11] L. Lu, W. Chen, *Adv. Mater.* **2010**, 22, 3745.
- [12] J. H. Jeon, R. K. Cheedarala, C. D. Kee, I. K. Oh, *Adv. Funct. Mater.* **2013**, 23, 6007.
- [13] M. Nan, D. Bang, S. Zheng, G. Go, B. A. Darmawan, S. Kim, H. Li, C. S. Kim, A. Hong, F. Wang, J. O. Park, E. Choi, *Sens. Actuators, B* **2020**, 323, 128709.
- [14] S. S. Kim, J. H. Jeon, H. Kim, C. D. Kee, I. K. Oh, *Adv. Funct. Mater.* **2015**, 25, 3560.
- [15] Z. Sun, L. Yang, D. Zhang, W. Song, *Sens. Actuators, B* **2019**, 283, 579.
- [16] I. S. Romero, N. P. Bradshaw, J. D. Larson, S. Y. Severt, S. J. Roberts, M. L. Schiller, J. M. Leger, A. R. Murphy, *Adv. Funct. Mater.* **2014**, 24, 3866.
- [17] S. Yun, J. Kim, *Carbon* **2011**, 49, 518.
- [18] J. H. Jeon, I. K. Oh, C. D. Kee, S. J. Kim, *Sens. Actuators, B* **2010**, 146, 307.
- [19] S. S. Kim, J. H. Jeon, C. D. Kee, I. K. Oh, *Smart Mater. Struct.* **2013**, 22, 085026.
- [20] F. Wang, Z. Jin, S. Zheng, H. Li, S. Cho, H. J. Kim, S. J. Kim, E. Choi, J. O. Park, S. Park, *Sens. Actuators, B* **2017**, 250, 402.
- [21] Y. Huang, C. Zhu, J. Yang, Y. Nie, C. Chen, D. Sun, *Cellulose* **2014**, 21, 1.
- [22] S. Wang, T. Li, C. Chen, W. Kong, S. Zhu, J. Dai, A. J. Diaz, E. Hitz, S. D. Solares, T. Li, L. Hu, *Adv. Funct. Mater.* **2018**, 28, 1707491.
- [23] F. Wang, J. H. Jeon, S. Park, C. D. Kee, S. J. Kim, I. K. Oh, *Soft Matter* **2016**, 12, 246.
- [24] A. Isogai, T. Hanninen, S. Fujisawa, T. Saito, *Prog. Polym. Sci.* **2018**, 86, 122.
- [25] F. Wang, H. J. Kim, S. Park, C. D. Kee, S. J. Kim, I. K. Oh, *Compos. Sci. Technol.* **2016**, 128, 33.
- [26] Y. Huang, H. Li, Z. Wang, M. Zhu, Z. Pei, Q. Xue, Y. Huang, C. Zhi, *Nano Energy* **2016**, 22, 422.
- [27] Y. Song, T. Liu, X. Xu, D. Feng, Y. Li, X. Liu, *Adv. Funct. Mater.* **2015**, 31, 4626.
- [28] W. Li, Z. Li, K. Bertelsmann, D. E. Fan, *Adv. Mater.* **2019**, 31, 1900720.
- [29] R. Hiraoki, Y. Ono, T. Saito, A. Isogai, *Biomacromolecules* **2015**, 16, 675.
- [30] R. Kubo, T. Saito, A. Isogai, *Cellulose* **2019**, 26, 4313.
- [31] J. Yang, X. Wang, B. Li, L. Ma, L. Shi, Y. Xiong, H. Xu, *Adv. Funct. Mater.* **2017**, 27, 1606497.
- [32] S. Kulandaivalu, Y. Sulaiman, *J. Power Sources* **2019**, 419, 181.
- [33] K. Jradi, B. Bideau, B. Chabot, C. Daneault, *J. Mater. Sci.* **2012**, 47, 3752.
- [34] Y. Q. Zhao, M. Lu, P. Y. Tao, Y. J. Zhang, X. T. Gong, Z. Yang, G. Q. Zhang, H. L. Li, *J. Power Sources* **2016**, 307, 391.
- [35] A. E. Jaouhari, S. B. Jadi, A. E. Guerra, M. Bouabdallaoui, Z. Aouzal, E. A. Bazzaoui, J. I. Martins, M. Bazzaoui, *Synth. Met.* **2018**, 245, 237.
- [36] Q. Yang, T. Saito, L. A. Berglund, A. Isogai, *Nanoscale* **2015**, 7, 17957.
- [37] F. Wang, J. H. Jeon, S. J. Kim, J. O. Park, S. Park, *J. Mater. Chem. B* **2016**, 4, 5015.
- [38] R. K. Cheedarala, J. H. Jeon, C. D. Kee, I. K. Oh, *Adv. Funct. Mater.* **2014**, 24, 6005.
- [39] M. Nan, F. Wang, S. Kim, H. Li, Z. Jin, D. Bang, C. S. Kim, J. O. Park, E. Choi, *Sens. Actuators, B* **2019**, 301, 127127.
- [40] M. Kotal, J. Kim, R. Tabassian, S. Roy, V. H. Nguyen, N. Koratkar, I. K. Oh, *Adv. Funct. Mater.* **2018**, 28, 1802464.
- [41] A. Simaite, B. Tondou, P. Soueres, C. Bergaud, *ACS Appl. Mater. Interfaces* **2015**, 7, 19966.
- [42] S. Umrao, R. Tabassian, J. Kim, Q. Zhou, S. Nam, I. K. Oh, *Sci. Robot.* **2019**, 4, eaaw7797.
- [43] J. Rivnay, S. Inal, B. A. Collins, M. Sessolo, E. Stavrinidou, X. Strakosas, C. Tassone, D. M. Delongchamp, G. G. Malliaras, *Nat. Commun.* **2016**, 7, 11287.
- [44] S. Savagatrup, E. Chan, S. M. Renteria-Garcia, A. D. Printz, A. V. Zaretski, T. F. Connor, D. Rodriguez, E. Valle, D. J. Lipomi, *Adv. Funct. Mater.* **2015**, 25, 427.